Mathematics

https://www.aimspress.com/journal/Math

AIMS Mathematics, 11(9): 30619–30642.
DOI:10.3934/math.20261213
Received: 05 July 2026
Revised: 02 September 2026
Accepted: 08 September 2026
Published: 20 September 2026

Research article

Mean-square spectral stability of stochastic FitzHugh–Nagumo networks with noise

Bing Zhou[1], **Manrui Zhou**[1], **Xiangrong Liu**[1] **and Qianqian Zheng**[2,*]

[1] School of Information Engineering, Zhongyuan Institute of Science and Technology, Xuchang 461000, China

[2] School of Science, Xuchang University, Xuchang 461000, China

* **Correspondence:** Email: zqq@xcu.edu.cn.

Abstract: This study investigates mean-square spectral instability in network-organized FitzHugh-Nagumo systems under multiplicative noise. By linearizing the stochastic dynamics and analyzing the spectrum of the second-moment operator, we state the exact mean-square stability condition and derive an explicit, generally conservative, spectral condition obtained with the Lyapunov choice $P = I$. The framework distinguishes direct noise acting on the membrane-potential variable, recovery-channel noise, and their combined influence. Numerical simulations illustrate how these noise channels and network connectivity change finite-network variability and synchronization diagnostics. Direct noise more strongly shifts the determinant component of the conservative spectral boundary in the parameter regimes studied, whereas recovery-channel noise produces a more gradual change. The results provide a mathematical and numerical framework for studying noise-dependent second-moment stability in excitable networks; they are not intended as evidence for clinical seizure regulation or as a demonstrated neuromodulation strategy.

Keywords: FitzHugh–Nagumo model; multiplicative noise; network; mean-square stability; synchronization
Mathematics Subject Classification: 34D20, 60H10, 92B20

1. Introduction

Spatiotemporal pattern formation is a fundamental phenomenon across biological, chemical, and ecological systems [1–3]. Since Turing's seminal work on diffusion-driven instability [4], studies of pattern formation have provided essential insights into how complex structures emerge from simple reaction–diffusion dynamics. Recent advances extend Turing theory to network-organized systems, where diffusion is represented by graph Laplacians, underscoring the decisive role of topology-such as node degree and spectral properties-in determining pattern onset and morphology [5–8]. Stochasticity is intrinsic to many real-world systems. Butler and Goldenfeld demonstrated that intrinsic noise can seed Turing patterns even when deterministic dynamics remain linearly stable [9], while Biancalani et al. showed that noise and finite-size effects fundamentally reshape dispersion and scaling [10]. Zhang and Zhou [11] established mean-square exponential stability results for stochastic reaction–diffusion systems under multiplicative noise, and Xiao et al. revealed that noise raises Turing thresholds in ecological networks, suppressing pattern formation and reducing hysteresis [12]. In neuronal contexts, Wang et al. investigated α-stable noise-induced chimera states in small-world Hindmarsh-Rose networks, showing that rewiring probability, noise stability parameter, and intensity govern incoherent domains, and proposed a local-order-parameter-based measure to quantify coherence [13]. Overall, these studies reflect a growing convergence of deterministic structure, network architecture, and stochastic effects in the modeling of excitable media. The FHN model, enriched by analytical depth and numerical sophistication, remains a central framework for probing synchronization, bifurcation, and pattern emergence in both theoretical neuroscience and nonlinear dynamics more broadly.

Related stochastic generalizations of network Turing theory have been developed previously. In particular, Asllani et al. studied stochastic Turing patterns on networks and showed how noise can seed or reshape pattern-forming modes in reaction-diffusion systems defined on complex graphs [14]. The present work differs in focus and methodology: we consider multiplicative noise acting on different components of the FitzHugh–Nagumo kinetics and derive explicit mean-square (second-moment) instability criteria that can be evaluated directly from the Laplacian spectrum and the local Jacobian/noise coefficients.

Recent developments in neural dynamics also include discrete and memristive neural models, which extend conventional continuous-time neuron descriptions by incorporating memory effects and richer nonlinear state coexistence. Discrete cascaded memristive neuron maps have been shown to exhibit hyperchaos and extreme multistability [15], while a recent review summarizes advances in discrete neuron models and memristive neural-network mappings, including multistability, synchronization transitions, and chimera dynamics [16]. Memristive Hopfield neural networks have also been exploited in time-series forecasting by using hidden heterogeneous and homogeneous extreme multistability to construct nonlinear initialization mechanisms [17]. These developments further illustrate how nonlinear mechanisms and network architecture can generate complex neural dynamics and provide a broader context for the stochastic FitzHugh–Nagumo framework considered here.

In realistic neural systems, intrinsic noise-arising from ion-channel gating, synaptic transmission, and cortical fluctuations is not only unavoidable but functionally significant. Such stochastic inputs can disrupt or enhance neural activity, promote synchronization, or induce coherent patterns absent in deterministic settings [18, 19]. The FitzHugh-Nagumo (FHN) model, a canonical reduction of the Hodgkin-Huxley system, remains central for studying excitability. Masoliver et al. showed that noise, delay, and topology jointly shape coherence in FHN networks [20], while Colombani and Le Bris established propagation of chaos and convergence to mean-field dynamics in large ensembles [21]. Gerster et al. reproduced seizure-like synchronization in brain-inspired FHN networks, identifying small-world connectivity as a key factor in seizure onset and termination [22]. Chouzouris et al. demonstrated that chimera states-coexisting synchronous and asynchronous groups-can mimic partial seizures, with hub removal mitigating epileptiform activity [23]. Extending this line, Cubillos Cornejo et al. mapped multiple dynamical regimes in small-world FHN networks, linking epileptic-like chimeras to randomness and coupling strength [24]. These findings highlight the broader role of chimera states in cortical networks, offering a framework to connect counterintuitive phenomena such as unihemispheric sleep with brain dynamics [25]. Moreover, coupled-oscillator models reveal that the collapse of coexisting synchronous and asynchronous oscillations into global synchronization-a mechanism associated with epileptic seizures-can arise from decreasing rather than increasing synchronization. Analyses of EEG recordings, together with closed-loop control experiments on chimera states, further demonstrate both the provocation and prevention of such outbreaks, offering new perspectives for seizure control and complex brain dynamics [26]. Han and Wang, et al, synthesized advances in network neurodynamics of epilepsy, covering hippocampal and BGCT circuit modeling, noise and delay effects, and DBS control, and shows that nonlinear dynamics both explains seizure transitions and guides targeted diagnosis and therapy [27–30]. Despite this progress, the second-moment behavior of networked stochastic systems-namely, MS Turing (in)stability that governs variance growth and pattern robustness-remains insufficiently explored. Addressing this gap, the present work derives explicit spectral conditions for MS Turing instability in network-organized FHN systems with multiplicative noise, disentangles direct (membrane) and indirect (channel-kinetic) noise pathways, and reveals how noise-topology interplay modulates pattern selection and synchronization.

The classical theory of Turing instability has profoundly shaped our understanding of pattern formation in spatially extended systems. However, real-world biological and neural systems are intrinsically noisy and organized over complex networks, where traditional deterministic frameworks fall short. While recent studies have demonstrated that stochastic fluctuations can induce or suppress Turing patterns, most of these focus on first-moment dynamics, offering limited insight into the variance and robustness of pattern formation. In particular, mean-square instability, which characterizes the growth of variance in system states, remains underexplored, despite its crucial importance in understanding fluctuation-driven transitions, reliability of spatial structures, and pathological phenomena such as seizure onset or abnormal synchrony. Furthermore, network topology, via its Laplacian spectrum and coupling architecture, interacts nontrivially with noise, potentially reshaping the bifurcation landscape in ways that deterministic models cannot capture.

In this study, we investigate the mean-square Turing instability in a generalized stochastic system defined on a random undirected graph and subject to multiplicative noise. We linearize the stochastic differential equations near a homogeneous steady state and derive explicit conditions for mean-square instability by analyzing the spectrum of the associated drift and diffusion matrices. Our theoretical framework reveals how noise injected into membrane potential (direct action) or ion-channel kinetics (indirect action) can independently or jointly reshape the stability landscape. Through numerical simulations, we compare direct, recovery-channel, and combined multiplicative noise and report their effects on the determinant component of the conservative spectral boundary, finite-network variability, and synchronization timing. These calculations provide mathematical and numerical diagnostics of noise-dependent second-moment behavior; they do not establish a clinical seizure-control mechanism or a demonstrated neuromodulation strategy.

2. The generalized network-organized systems with independent multiplicative noise

We consider a two-component reaction–diffusion system on an undirected graph. To avoid the sign ambiguity raised by different Laplacian conventions, we use

$$L = \mathcal{A} - \mathcal{D} = -\mathcal{L},$$

where $\mathcal{A}$ is the adjacency matrix, $\mathcal{D}$ is the degree matrix, and $\mathcal{L} = \mathcal{D} - \mathcal{A}$ is the standard positive semidefinite graph Laplacian. Thus $L = L^T$ is negative semidefinite and

$$0 = \Lambda_1 \geq \Lambda_2 \geq \cdots \geq \Lambda_n, \qquad \mu_k = -\Lambda_k \geq 0.$$

With this convention, physical diffusion is represented by adding L to the reaction kinetics. For example,

$$\sum_{j=1}^{n} L_{ij} u_j = \sum_{j\sim i} \mathcal{A}_{ij}(u_j - u_i),$$

so a node with a value larger than its neighbours receives a negative diffusive contribution. This is the sign convention used in both the analytical derivation and the simulations.

A stochastic network-organized system with local independent multiplicative noise is written as

$$\begin{cases} du_i = \left[f(u_i, v_i) + \sum_{j=1}^{n} L_{ij}\phi(u_j) \right] dt + F(u_i - u^*)\, dW_i^{(u)}(t), \\ dv_i = \left[g(u_i, v_i) + \sum_{j=1}^{n} L_{ij}\varphi(v_j) \right] dt + G(v_i - v^*)\, dW_i^{(v)}(t), \end{cases} \tag{2.1}$$

where (u^*, v^*) is the homogeneous equilibrium satisfying $f(u^*, v^*) = g(u^*, v^*) = 0$. The Brownian motions $\{W_i^{(u)}(t), W_i^{(v)}(t)\}_{i=1}^{n}$ are mutually independent standard Brownian motions. This choice models local intrinsic fluctuations and avoids the artificial alignment that can be produced by a single Brownian driver shared by all nodes and all variables. The noise intensities are functions of perturbations from the equilibrium, so the stochastic forcing vanishes at (u^*, v^*); otherwise an additive stochastic term would remain at the equilibrium and an equilibrium-based mean-square stability analysis would be inconsistent.

Let $u = (u_1 - u^*, \ldots, u_n - u^*)^T$, $v = (v_1 - v^*, \ldots, v_n - v^*)^T$, and $\theta = (u^T, v^T)^T$. Denote the partial derivatives at the homogeneous equilibrium by $f_u, f_v, g_u, g_v, \phi_u, \varphi_v, F_u, G_v$. The linearized multi-channel Itô system is

$$d\theta = J\theta\, dt + \sum_{i=1}^{n} B_i^{(u)}\theta\, dW_i^{(u)}(t) + \sum_{i=1}^{n} B_i^{(v)}\theta\, dW_i^{(v)}(t), \tag{2.2}$$

where the drift matrix is denoted by J to avoid confusion with the adjacency matrix,

$$J = \begin{pmatrix} f_u I + \phi_u L & f_v I \\ g_u I & g_v I + \varphi_v L \end{pmatrix}, \quad B_i^{(u)} = \begin{pmatrix} F_u E_i & 0 \\ 0 & 0 \end{pmatrix}, \quad B_i^{(v)} = \begin{pmatrix} 0 & 0 \\ 0 & G_v E_i \end{pmatrix}.$$

Here $E_i = e_i e_i^T$, and e_i is the i-th unit vector in $\mathbb{R}^n$. Since the noises are independent,

$$\sum_{i=1}^{n} \left[(B_i^{(u)})^T B_i^{(u)} + (B_i^{(v)})^T B_i^{(v)} \right] = \begin{pmatrix} F_u^2 I & 0 \\ 0 & G_v^2 I \end{pmatrix}. \tag{2.3}$$

For $H(\theta) = ||\theta||^2$, Itô's formula gives

$$\frac{d}{dt}E||\theta(t)||^2 = E\left[\theta^T\left(J^T + J + \sum_{i=1}^{n}((B_i^{(u)})^T B_i^{(u)} + (B_i^{(v)})^T B_i^{(v)})\right)\theta\right]. \tag{2.4}$$

The full mean-square exponential stability problem is governed by the second-moment equation. If $\Sigma(t) = E[\theta(t)\theta(t)^T]$, then

$$\frac{d}{dt}\operatorname{vec}\Sigma = \mathcal{K}\operatorname{vec}\Sigma,$$

where

$$\mathcal{K} = I_{2n}\otimes J + J\otimes I_{2n} + \sum_{i=1}^{n}\left(B_i^{(u)}\otimes B_i^{(u)} + B_i^{(v)}\otimes B_i^{(v)}\right). \tag{2.5}$$

Thus the rigorous mean-square stability condition is

$$s(\mathcal{K}) := \max\{\operatorname{Re}\lambda : \lambda\in\sigma(\mathcal{K})\} < 0, \tag{2.6}$$

and exact mean-square instability occurs when $s(\mathcal{K}) > 0$.

Mean-square stability and Turing-type instability. Let $\Pi_0 = I_2\otimes(n^{-1}\mathbf{1}\mathbf{1}^T)$ and $\Pi_\perp = I_{2n} - \Pi_0$ denote the homogeneous and heterogeneous projections, respectively. The homogeneous equilibrium is called mean-square exponentially stable if there exist constants $C \geq 1$ and $\gamma > 0$ such that

$$E||\theta(t)||^2 \leq Ce^{-\gamma t}||\theta(0)||^2 \quad \text{for every deterministic } \theta(0). \tag{2.7}$$

For the linear Itô system (2.2), this property is equivalent to $s(\mathcal{K}) < 0$. We call the equilibrium mean-square spectrally unstable when $s(\mathcal{K}) > 0$. To reserve the word "Turing" for spatial symmetry breaking, we use mean-square Turing-type instability only when the uncoupled homogeneous kinetics is mean-square stable but there exists an initial perturbation with $\Pi_\perp\theta(0) \neq 0$ for which

$$\limsup_{t\to\infty}\frac{1}{t}\log E||\Pi_\perp\theta(t)||^2 > 0. \tag{2.8}$$

Because node-wise independent noises do not leave the deterministic Laplacian-mode subspaces invariant, the exact operator $\mathcal{K}$ generally couples modal covariances. Consequently, $s(\mathcal{K}) > 0$ proves total mean-square instability but, by itself, does not prove Turing-type spatial selection in the sense of (2.8); the heterogeneous projected covariance must also be examined. Within the conservative $P = I$ modal diagnostic, the corresponding sufficient Turing-type indication is $\rho(0) < 0$ together with $\rho(\Lambda_k) > 0$ for at least one $k \geq 2$.

A standard Lyapunov sufficient stability certificate is the existence of $P > 0$ satisfying

$$J^TP + PJ + \sum_{i=1}^{n}\left[(B_i^{(u)})^T PB_i^{(u)} + (B_i^{(v)})^T PB_i^{(v)}\right] \prec 0. \tag{2.9}$$

The special choice $P = I$ gives a transparent but generally conservative stability bound. Here P is the positive-definite weighting matrix in the quadratic Lyapunov function $V(\theta) = \theta^T P\theta$, and $P = I$ means that the standard Euclidean energy $V(\theta) = ||\theta||^2$ is used without introducing additional directional weights. This choice makes the stability condition explicitly reducible to Laplacian modes, but it is more restrictive than allowing an arbitrary $P > 0$ and is therefore generally conservative. Therefore, in what follows, the Laplacian-mode condition derived from $P = I$ is used as an explicit spectral indicator and not as a necessary-and-sufficient mean-square instability theorem for all non-normal systems.

Let Θ be an orthogonal matrix that diagonalizes L, namely $\Theta^T L\Theta = \mathrm{diag}(\Lambda_1, \ldots, \Lambda_n)$. Throughout this paper Λ_k denotes an eigenvalue of L, not of $L + L^T$. For the $P = I$ bound, the symmetric matrix in (2.4) becomes block diagonal in the Laplacian-eigenmode basis. The k-th 2×2 mode matrix is

$$M(\Lambda_k) = \begin{pmatrix} 2(f_u + \phi_u\Lambda_k) + F_u^2 & f_v + g_u \\ f_v + g_u & 2(g_v + \varphi_v\Lambda_k) + G_v^2 \end{pmatrix}. \tag{2.10}$$

The sign of the coupling term is consistent with (2.1): since $\Lambda_k \le 0$ and $\phi_u, \varphi_v > 0$, diffusion contributes negatively to the diagonal entries.

Define

$$\rho(\Lambda_k) = \lambda_{\max}(M(\Lambda_k)), \quad \alpha(\Lambda_k) = \mathrm{tr}\, M(\Lambda_k), \quad \beta(\Lambda_k) = \det M(\Lambda_k). \tag{2.11}$$

The sufficient $P = I$ mean-square stability condition is $\rho(\Lambda_k) < 0$ for every k. Since $M(\Lambda_k)$ is a real symmetric 2×2 matrix, the corresponding conservative prediction of mode growth is

$$\rho(\Lambda_k) > 0, \tag{2.12}$$

which is equivalently expressed by

$$\beta(\Lambda_k) < 0 \quad \text{or} \quad (\beta(\Lambda_k) \ge 0 \text{ and } \alpha(\Lambda_k) > 0). \tag{2.13}$$

The boundary of this $P = I$ spectral indicator is $\rho(\Lambda_k) = 0$; when the crossing occurs from a negative-definite mode matrix, this reduces to $\beta(\Lambda_k) = 0$ with $\alpha(\Lambda_k) \le 0$.

For the FitzHugh–Nagumo example used below, $\phi_u = d_1$, $\varphi_v = d_2$, $F_u = D_1$, and $G_v = D_2$. Hence,

$$\alpha(\Lambda; D_1, D_2, d_1, d_2) = 2(f_u + d_1\Lambda) + 2(g_v + d_2\Lambda) + D_1^2 + D_2^2, \tag{2.14}$$

$$\beta(\Lambda; D_1, D_2, d_1, d_2) = [2(f_u + d_1\Lambda) + D_1^2][2(g_v + d_2\Lambda) + D_2^2] - (f_v + g_u)^2. \tag{2.15}$$

Equivalently,

$$\beta(\Lambda) = 4d_1d_2\Lambda^2 + \left(2d_1(2g_v + D_2^2) + 2d_2(2f_u + D_1^2)\right)\Lambda + (2f_u + D_1^2)(2g_v + D_2^2) - (f_v + g_u)^2. \tag{2.16}$$

The last term is $(f_v + g_u)^2$ because β is the determinant of the symmetric matrix $M(\Lambda)$ in (2.10), not the determinant of the deterministic Jacobian. Equations (2.14)–(2.16) explicitly show how the conservative instability boundary depends on multiplicative-noise intensity and diffusivity contrast. In a regular lattice, Λ is a function of the spatial wave number; on a general graph, Λ_k is the discrete analogue of a wave-number-dependent mode.

Determinant-based instability interval. Since the numerical spectral panels below are drawn in terms of the determinant indicator $\beta(\Lambda)$, we record the corresponding interval condition explicitly. Write

$$\beta(\Lambda) = a_\beta\Lambda^2 + b_\beta\Lambda + c_\beta, \tag{2.17}$$

where

$$a_\beta = 4d_1d_2, \quad b_\beta = 2d_1(2g_v + D_2^2) + 2d_2(2f_u + D_1^2), \tag{2.18}$$

and

$$c_\beta = (2f_u + D_1^2)(2g_v + D_2^2) - (f_v + g_u)^2. \tag{2.19}$$

If $d_1d_2 > 0$ and

$$\Delta_\beta = b_\beta^2 - 4a_\beta c_\beta > 0, \tag{2.20}$$

then $\beta(\Lambda) = 0$ has two real roots

$$\lambda_4 = \frac{-b_\beta - \sqrt{\Delta_\beta}}{2a_\beta}, \qquad \lambda_5 = \frac{-b_\beta + \sqrt{\Delta_\beta}}{2a_\beta}, \qquad \lambda_4 < \lambda_5. \tag{2.21}$$

Since $a_\beta > 0$, the determinant indicator satisfies

$$\beta(\Lambda) < 0 \quad \Longleftrightarrow \quad \Lambda \in (\lambda_4, \lambda_5). \tag{2.22}$$

Therefore, for a finite graph with eigenvalues $0 = \Lambda_1 \geq \Lambda_2 \geq \cdots \geq \Lambda_n$, the determinant-unstable modes are those graph modes whose eigenvalues fall into the interval (λ_4, λ_5). The diagnostic count used in the numerical plots is

$$N_{\text{unst}}^{\beta} = \#\{k \in \{1, \ldots, n\} : \beta(\Lambda_k) < 0\} = \#\{k : \Lambda_k \in (\lambda_4, \lambda_5)\}. \tag{2.23}$$

Only the intersection of (λ_4, λ_5) with the non-positive graph spectrum is relevant, because the eigenvalues of $L = \mathcal{A} - \mathcal{D}$ satisfy $\Lambda_k \leq 0$.

Relation between $\beta(\Lambda)$ and the $P = I$ spectral bound. For the symmetric 2×2 matrix $M(\Lambda)$, the condition $\beta(\Lambda) < 0$ means that the two eigenvalues of $M(\Lambda)$ have opposite signs. Hence,

$$\beta(\Lambda) < 0 \quad \Longrightarrow \quad \rho(\Lambda) > 0. \tag{2.24}$$

Thus, $\beta(\Lambda) < 0$ is a simple determinant-based sufficient indicator for the loss of the $P = I$ mean-square stability bound. The full $P = I$ criterion also includes the trace-driven case $\beta(\Lambda) \geq 0$ and $\alpha(\Lambda) > 0$. In the numerical figures, we focus on the determinant branch $\beta(\Lambda) < 0$ because the plotted instability intervals λ_4 and λ_5 are obtained from $\beta(\Lambda) = 0$.

How multiplicative noise shifts the determinant boundary. The dependence of the determinant indicator on the two noise intensities can be seen from

$$\beta(\Lambda) = A_u(\Lambda)A_v(\Lambda) - (f_v + g_u)^2, \tag{2.25}$$

where

$$A_u(\Lambda) = 2(f_u + d_1\Lambda) + D_1^2, \qquad A_v(\Lambda) = 2(g_v + d_2\Lambda) + D_2^2. \tag{2.26}$$

Differentiating with respect to D_1^2 and D_2^2 gives

$$\frac{\partial \beta}{\partial D_1^2} = A_v(\Lambda) = 2(g_v + d_2\Lambda) + D_2^2, \qquad \frac{\partial \beta}{\partial D_2^2} = A_u(\Lambda) = 2(f_u + d_1\Lambda) + D_1^2. \tag{2.27}$$

These expressions show that direct noise D_1 and recovery-channel noise D_2 move the determinant boundary through different diagonal entries of the mode matrix. If $A_v(\Lambda) < 0$, increasing D_1 decreases $\beta(\Lambda)$ and can move additional graph modes into the determinant-negative interval. Similarly, the effect of D_2 is governed by the sign and magnitude of $A_u(\Lambda)$. This provides a theoretical explanation for why the two multiplicative-noise channels may have different effects on the number of determinant-unstable modes and on finite-network synchronization diagnostics.

Mode-wise critical noise intensities. For a fixed graph mode Λ_k and fixed D_2, the determinant boundary $\beta(\Lambda_k) = 0$ can be solved formally for the critical direct-noise intensity:

$$D^2_{1,c}(\Lambda_k; D_2) = \frac{(f_v + g_u)^2}{2(g_v + d_2\Lambda_k) + D_2^2} - 2(f_u + d_1\Lambda_k), \tag{2.28}$$

provided that $2(g_v+d_2\Lambda_k)+D_2^2 \neq 0$. Similarly, for fixed D_1, the critical recovery-channel noise intensity is

$$D^2_{2,c}(\Lambda_k; D_1) = \frac{(f_v + g_u)^2}{2(f_u + d_1\Lambda_k) + D_1^2} - 2(g_v + d_2\Lambda_k), \tag{2.29}$$

provided that $2(f_u + d_1\Lambda_k) + D_1^2 \neq 0$. Only nonnegative values of $D^2_{1,c}$ and $D^2_{2,c}$ are physically admissible. These mode-wise thresholds give explicit noise-dependent boundaries and complement the root representation in (2.21).

3. Results and discussion

We now apply the above criterion to a stochastic FitzHugh–Nagumo network. With the sign convention $L = \mathcal{A} - \mathcal{D}$, the model used in the simulations is

$$\begin{cases} du_i = \left[u_i - \dfrac{u_i^3}{3} - v_i + I + d_1 \displaystyle\sum_{j=1}^{n} L_{ij} u_j \right] dt + D_1(u_i - u^*)\, dW_i^{(u)}(t), \\ dv_i = \left[\varepsilon(u_i + a - bv_i) + d_2 \displaystyle\sum_{j=1}^{n} L_{ij} v_j \right] dt + D_2(v_i - v^*)\, dW_i^{(v)}(t), \end{cases} \tag{3.1}$$

where the Brownian motions are independent for different nodes and different variables. The homogeneous equilibrium (u^*, v^*) is determined by

$$u^* - \frac{(u^*)^3}{3} - v^* + I = 0, \qquad u^* + a - bv^* = 0,$$

and the Laplacian terms vanish because each row of L sums to zero. For this model,

$$f_u = 1 - (u^*)^2, \qquad f_v = -1, \qquad g_u = \varepsilon, \qquad g_v = -\varepsilon b.$$

Unless otherwise stated, the fixed parameters are $a = 0.7$, $b = 0.8$, $\varepsilon = 0.08$, $n = 100$, and $d_1 = d_2 = 0.1$. The network is an Erdős–Rényi graph $G(n, p)$. The connection probability p changes the Laplacian spectrum and therefore changes which graph modes may enter the predicted unstable interval. When $d_1 = d_2$, the deterministic diffusivity contrast is absent; the computations should therefore be interpreted as noise-modulated mean-square spectral stability and synchronization, not as a complete demonstration of classical continuous-space Turing patterns. To analyze a genuine diffusivity-driven Turing boundary, one should also scan (d_1, d_2) and verify that the homogeneous equilibrium is stable without diffusion but unstable for a nonzero graph mode. More precisely, classical Turing instability requires a homogeneous equilibrium that is stable in the uncoupled deterministic kinetics but destabilized by a nonhomogeneous spatial mode through differential diffusion. The present calculations mainly use $d_1 = d_2$ and therefore do not satisfy the usual diffusivity-contrast mechanism. In this setting, “Turing” is used only in the broader graph-modal sense of a nonhomogeneous second-moment mode crossing a spectral boundary. To avoid ambiguity, we describe the reported effect below as noise-modulated mean-square spectral instability unless the classical requirements have been checked explicitly.

Trace-driven branch for the adopted FHN setting. For $I = 0.25$, the equilibrium is $u^* = -1.032480$ and hence $f_u = -0.0660154$, while $g_v = -0.064$. Write

$$A_u(\Lambda) = D_1^2 - 0.1320308 + 0.2\Lambda, \qquad A_v(\Lambda) = D_2^2 - 0.128 + 0.2\Lambda.$$

Since $M(\Lambda)$ is symmetric, the trace-driven condition $\beta(\Lambda) \geq 0$ and $\alpha(\Lambda) > 0$ is equivalent to $M(\Lambda)$ being positive semidefinite with at least one positive eigenvalue. In the present 2×2 case this requires

$$A_u(\Lambda) > 0, \qquad A_v(\Lambda) > 0, \qquad A_u(\Lambda)A_v(\Lambda) \geq (f_v + g_u)^2 = 0.8464. \tag{3.2}$$

Because $\Lambda \leq 0$ and $d_1 = d_2 = 0.1$, both diagonal terms are maximized by the homogeneous mode $\Lambda_1 = 0$. Therefore, if any graph mode satisfies the trace-driven condition, the homogeneous mode satisfies it as well. The trace-driven region is thus characterized by

$$D_1^2 > 0.1320308, \quad D_2^2 > 0.128, \quad (D_1^2 - 0.1320308)(D_2^2 - 0.128) \geq 0.8464. \tag{3.3}$$

It is absent in every one-channel sweep with $D_1 = 0$ or $D_2 = 0$ and is also absent for $0 \leq D_1, D_2 \leq 0.6$. It can occur in the wider combined-noise domain used in Figure 6; for example, along $D_1 = D_2 = D$ the boundary is $D \approx 1.02470$. Such a crossing first destabilizes the homogeneous mode and is therefore not a purely nonhomogeneous Turing-type instability. Accordingly, determinant-root plots alone are exhaustive for the one-channel diagnostics shown below, but the full criterion (2.13) must be used in the high-intensity combined-noise region. The values $a = 0.7$, $b = 0.8$, and $\varepsilon = 0.08$ are widely used in FitzHugh–Nagumo studies and have also been adopted in coupled FHN lattice models [31]. Since the FHN variables and parameters are dimensionless, these values should be interpreted phenomenologically rather than as direct ion-channel measurements. In particular, $\varepsilon = 0.08 \ll 1$ preserves the characteristic fast-slow separation between the membrane-potential variable u and the recovery variable v. The external current I is then varied to place the local kinetics either below the lower Hopf threshold or in the oscillatory regime, as quantified below, allowing the effect of multiplicative noise to be distinguished from a change of the intrinsic local dynamical regime.

Because the spectral panels in Figures 1, 2, 4, 6, 7, and 9 plot the determinant indicator $\beta(\Lambda)$, the reported number of unstable modes in the numerical figures is defined by

$$N_{\text{unst}}^{\beta} = \#\{k \in \{1, \ldots, n\} : \beta(\Lambda_k) < 0\}. \tag{3.4}$$

This determinant-based count corresponds to the determinant branch of the $P = I$ criterion in (2.13) and is the quantity displayed in the diagnostic panels; it is also consistent with the interval formula (2.23). The full conservative $P = I$ loss-of-stability indicator is given by $\rho(\Lambda_k) > 0$, or equivalently by (2.13); therefore, when $\beta(\Lambda_k) \geq 0$ and $\alpha(\Lambda_k) > 0$, this additional trace-driven case should be checked separately. In the parameter regimes shown below, the plotted instability intervals are determined by the roots of $\beta(\Lambda) = 0$.

The stochastic simulations are performed with the Euler–Maruyama method. At each time step, independent increments $\Delta W_i^{(u)}$ and $\Delta W_i^{(v)}$ are generated as normal random variables with mean zero and variance Δt. The baseline time step is $\Delta t = 0.01$. Initial data are small heterogeneous perturbations of (u^*, v^*) so that the early dynamics can be compared with the linear spectral prediction. The time-series panels are used as representative finite-network stochastic responses after the determinant boundary is crossed.

For the deterministic baseline in Figure 1, panels (a)–(d) use the same fixed adjacency matrix, Laplacian spectrum, deterministic parameters, and initial heterogeneous perturbation. The only change between panels (a)–(b) and panels (c)–(d) is the direct multiplicative-noise intensity, from $D_1 = 0$ to $D_1 = 0.1$ with $D_2 = 0$. Thus the comparison isolates the effect of multiplicative noise without a topology or initial-condition confound.

To compare the exact condition (2.6) with the $P = I$ spectral indicator directly, we evaluated both quantities on a reproducible connected Erdős–Rényi graph with $n = 10$, $p = 0.35$, and random seed 314159. The smaller graph is used because the exact operator $\mathcal{K}$ has dimension $(2n)^2 \times (2n)^2$, whereas evaluation of the $P = I$ modal bound requires only 2×2 matrices. Table 1 shows representative direct- and recovery-channel-noise cases. Negative $s(\mathcal{K})$ gives exact mean-square stability, while $\max_k \rho(\Lambda_k) < 0$ would certify stability under $P = I$. The exact calculation remains stable for cases A–D and becomes unstable in case E. In contrast, the $P = I$ quantity is positive in all five cases. Thus the comparison confirms both the exact transition detected by $s(\mathcal{K})$ and the conservatism of the Euclidean Lyapunov certificate: failure of the $P = I$ test must not be interpreted as exact instability.

Table 1. Comparison of the exact second-moment spectral abscissa and the conservative $P = I$ indicator. Fixed parameters are $a = 0.7$, $b = 0.8$, $\varepsilon = 0.08$, $I = 0.25$, $d_1 = d_2 = 0.1$, $n = 10$, $p = 0.35$, and graph seed 314159.

Case	D_1	D_2	$s(\mathcal{K})$	$\max_k \rho(\Lambda_k)$	Exact state
A	0.00	0.00	−0.130015	0.789987	stable
B	0.10	0.00	−0.129509	0.794989	stable
C	0.00	0.10	−0.129509	0.795011	stable
D	0.20	0.00	−0.127900	0.810160	stable
E	0.80	0.00	0.134888	1.163388	unstable

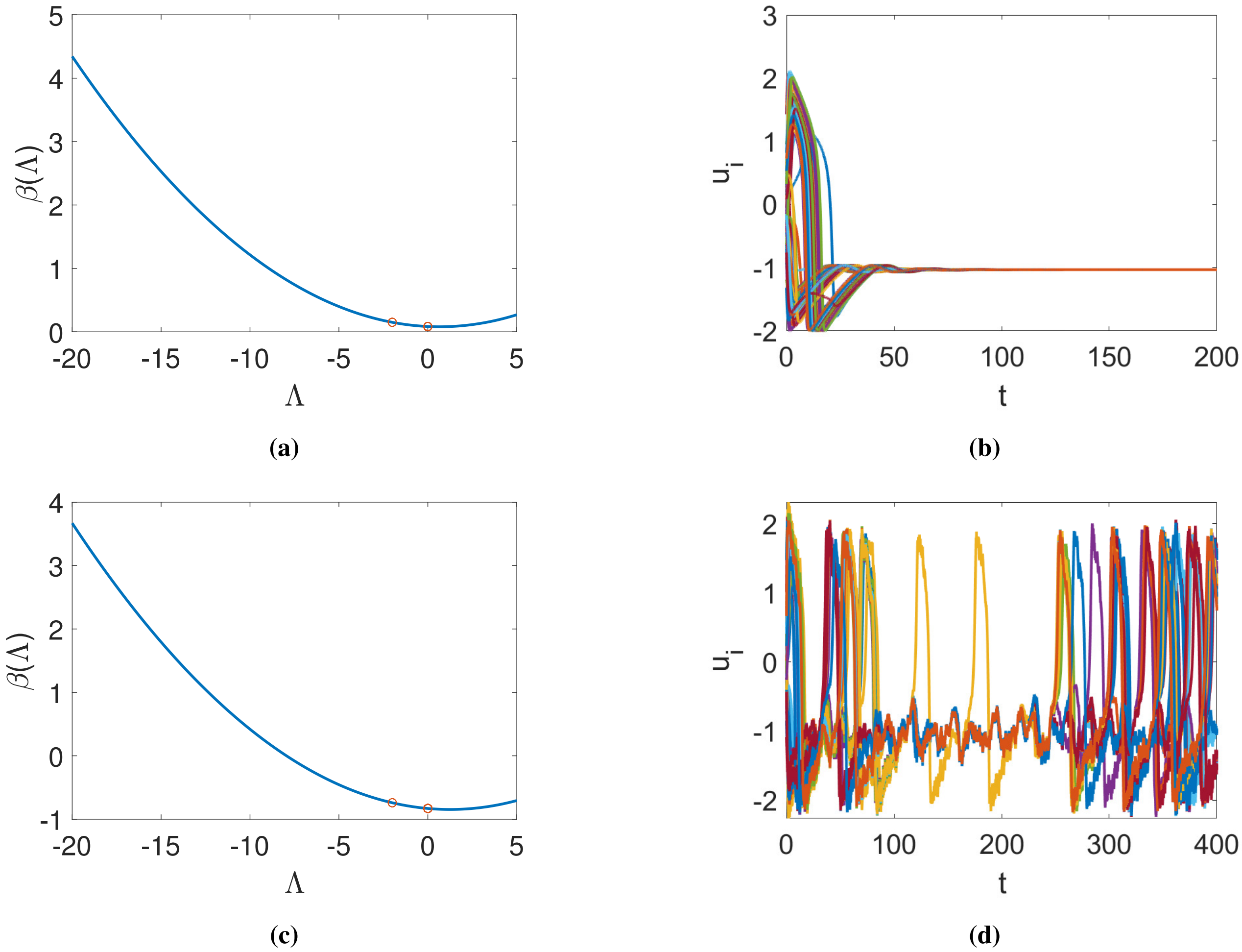

Figure 1. Determinant-based spectral indicator and stochastic response of system (3.1) when $I = 0.25$. (a) The determinant indicator $\beta(\Lambda) = \det M(\Lambda)$ as a function of the Laplacian eigenvalue Λ when $p = 0.005$ and $D_1 = D_2 = 0$; the marked points denote the graph eigenvalues Λ_k of the displayed network realization. (b) Representative node time series when $p = 0.005$ and $D_1 = D_2 = 0$. (c) The determinant indicator $\beta(\Lambda)$ when $p = 0.005$, $D_1 = 0.1$, and $D_2 = 0$; graph modes located in the interval $\beta(\Lambda_k) < 0$ are identified as determinant-unstable modes under the $P = I$ spectral indicator. (d) Representative node time series when $p = 0.005$, $D_1 = 0.1$, and $D_2 = 0$. All four panels use the same fixed network topology and initial perturbation; only D_1 changes between the deterministic and noisy cases. The fixed parameters are $a = 0.7$, $b = 0.8$, $\varepsilon = 0.08$, $n = 100$, $d_1 = d_2 = 0.1$, and $I = 0.25$.

For the additional uncertainty analysis in Figure 13, we used 30 independent stochastic realizations on one fixed connected graph ($n = 100$, $p = 0.05$, graph seed 20260828) and independent Brownian seeds 1000–1029. The shaded band is the pointwise empirical 2.5–97.5 percentile interval and the solid curve is the pointwise median. A time-step check was performed with $\Delta t = 0.02$, 0.01, and 0.005. The ensemble mean of the time-averaged STD over $15 \le t \le 20$ was 4.7176×10^{-4}, 4.6408×10^{-4}, and 4.8383×10^{-4}, respectively; the corresponding 95% confidence-interval half-widths were 6.073×10^{-5}, 5.584×10^{-5}, and 6.533×10^{-5}. These overlapping intervals indicate that the reported ensemble diagnostic is not materially changed by halving the baseline step.

To separate graph-to-graph and path-to-path fluctuations from the mean noise-intensity trend, Figure 14 uses 20 independent connected $G(100, 0.05)$ graph realizations and an independent Brownian path for every graph and every value $D_1 = 0, 0.1, \ldots, 1.0$; $D_2 = 0$ and $\Delta t = 0.01$. For each replicate, N^{β}_{unst} is recomputed from that graph's spectrum, PST is computed from the corresponding trajectory, and the scalar STD diagnostic is the time average over $10 \le t \le 15$. Curves show ensemble means and error bars show 95% confidence intervals. The graph-dependent mode count has relatively narrow intervals and increases systematically from 44.30 ± 1.42 at $D_1 = 0$ to 74.35 ± 1.27 at $D_1 = 1$. The PST and STD diagnostics show visibly larger relative uncertainty, especially at high noise intensity, because they depend on both the graph realization and the Brownian sample. Nevertheless, their ensemble means retain the overall increase with D_1. This comparison shows why a single stochastic path should be treated as illustrative rather than as an ensemble estimate.

To quantify finite-network heterogeneity and synchronization, we use

$$\text{STD}(t) = \sqrt{\frac{1}{n}\sum_{j=1}^{n}\left(u_j(t) - \bar{u}(t)\right)^2}, \qquad \text{STD}_v(t) = \sqrt{\frac{1}{n}\sum_{j=1}^{n}\left(v_j(t) - \bar{v}(t)\right)^2}, \tag{3.5}$$

where $\bar{u}(t) = n^{-1}\sum_{j=1}^{n} u_j(t)$ and $\bar{v}(t) = n^{-1}\sum_{j=1}^{n} v_j(t)$. Large values indicate node-to-node heterogeneity, whereas values close to zero indicate synchronization. We also record a potential switching count PST, defined as the number of episodes in which $\text{STD}(t)$ rises above $\eta_{\text{sw}} = 10^{-2}$ and later drops below it, and a synchronization time ST, defined as the first time after which $\text{STD}(t) \le \eta_{\text{syn}} = 10^{-3}$ remains satisfied over the rest of the simulated time interval. The switching threshold $\eta_{\text{sw}} = 10^{-2}$ is chosen to match the order of the imposed initial node-to-node perturbation and therefore separates macroscopic excursions from small residual dispersion. The synchronization threshold $\eta_{\text{syn}} = 10^{-3}$ is one order of magnitude smaller, so "synchronized" means that dispersion has decayed well below its initial level. These values are operational numerical tolerances, not bifurcation constants. Consequently, the absolute values of PST and ST are threshold-dependent, especially when a trajectory remains close to a threshold. We therefore use them only as comparative diagnostics, report the underlying $\text{STD}(t)$ curves, and regard a trend as robust only when it persists under the sensitivity ranges $\eta_{\text{sw}} \in [5 \times 10^{-3}, 2 \times 10^{-2}]$ and $\eta_{\text{syn}} \in [5 \times 10^{-4}, 2 \times 10^{-3}]$. Near-threshold cases should be interpreted with the ensemble uncertainty band rather than from a single count or crossing time.

The external current I is a primary bifurcation parameter of the local FHN kinetics. For $a = 0.7$, $b = 0.8$, and $\varepsilon = 0.08$, the local equilibrium changes stability when

$$1 - (u^*)^2 - \varepsilon b = 0,$$

which gives $u^* = \pm\sqrt{1 - \varepsilon b}$ and the corresponding currents

$$I_H^{(1)} \approx 0.3313, \qquad I_H^{(2)} \approx 1.4187.$$

Thus, $I = 0.25$ is used for the equilibrium-based spectral stability tests below the lower Hopf threshold, whereas $I = 0.5$ lies in an oscillatory regime and is used only for synchronization diagnostics of nonlinear oscillations. Results obtained at these two currents should not be conflated.

The first group of simulations compares the determinant-based spectral prediction with stochastic trajectories near the homogeneous equilibrium. For $D_1 = D_2 = 0$, the marked graph eigenvalues lie outside the determinant-negative interval and the trajectory relaxes toward the homogeneous state (Figures 1(a) and 1(b)). When $D_1 = 0.1$ and $D_2 = 0$, the curve $\beta(\Lambda)$ is shifted downward and several graph eigenvalues satisfy $\beta(\Lambda_k) < 0$ (Figure 1(c)); the corresponding time series show increased node-to-node variability (Figure 1(d)). When $p = 0.1$, more instability modes emerge (Figure 2(a)), leading system (3.1) to rapidly transition into synchronous oscillations (Figure 2(b)). A comparison between Figures 1(d) and 2(b) suggests that the link probability p plays a crucial role in modulating synchronous behavior.

For larger connection probability p, the graph spectrum spreads over a wider range of Λ_k, so more modes may enter the determinant-negative interval. With $D_2 = 0$, increasing D_1 enlarges this interval and generally increases both N^{β}_{unst} and the switching count PST (Figure 3(a)). The STD diagnostic also increases (Figure 3(b)), indicating stronger finite-network heterogeneity. Thus, direct multiplicative noise in the activator-like variable has a stronger influence on the determinant component of the $P = I$ spectral bound.

When noise acts only on the recovery variable ($D_1 = 0$, $D_2 > 0$), the curve $\beta(\Lambda)$ and its roots change more gradually (Figure 4). The curves in Figure 5 indicate that recovery-channel noise mainly adjusts variability and synchronization timing. The comparison between Figures 3(b) and 5(b) should be interpreted carefully: direct noise more clearly increases the number of determinant-unstable modes, while the STD amplitude can be comparable for the two channels and may increase at different rates depending on the parameter scale.

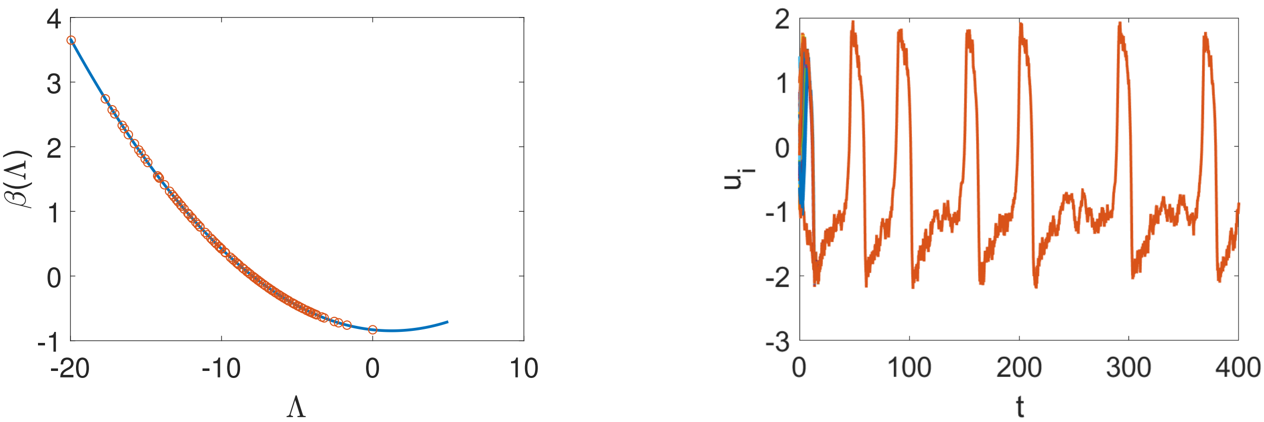

(a) **(b)**

Figure 2. Determinant-based spectral indicator and stochastic response of system (3.1) when $D_1 = 0.1$, $D_2 = 0$, and $I = 0.25$. (a) The determinant indicator $\beta(\Lambda) = \det M(\Lambda)$ as a function of the Laplacian eigenvalue Λ; the marked points denote the graph eigenvalues Λ_k. (b) Representative node time series showing the finite-network stochastic response. The fixed parameters are $a = 0.7$, $b = 0.8$, $\varepsilon = 0.08$, $n = 100$, $d_1 = d_2 = 0.1$, and $I = 0.25$.

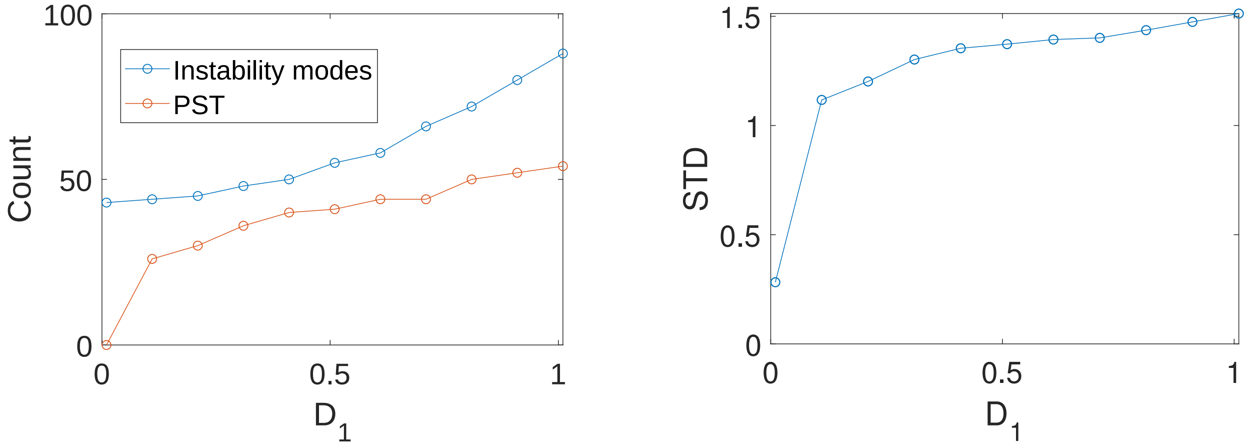

(a) **(b)**

Figure 3. Noise-intensity dependence for direct noise when $D_2 = 0$. (a) Diagnostic curves for the number of determinant-unstable modes N^{β}_{unst}, defined by $\beta(\Lambda_k) < 0$, and the potential switching count PST as functions of D_1. (b) Diagnostic curve for STD as a function of D_1. The left vertical axis is labeled "Count", and the right vertical axis is labeled "STD", consistently with (3.5). The fixed parameters are $a = 0.7$, $b = 0.8$, $\varepsilon = 0.08$, $n = 100$, $d_1 = d_2 = 0.1$, and $I = 0.25$. Here N^{β}_{unst} counts the graph modes satisfying $\beta(\Lambda_k) < 0$, PST counts the episodes in which STD rises above 10^{-2} and subsequently returns below this threshold, and STD measures the node-to-node dispersion of the membrane-potential variable u.

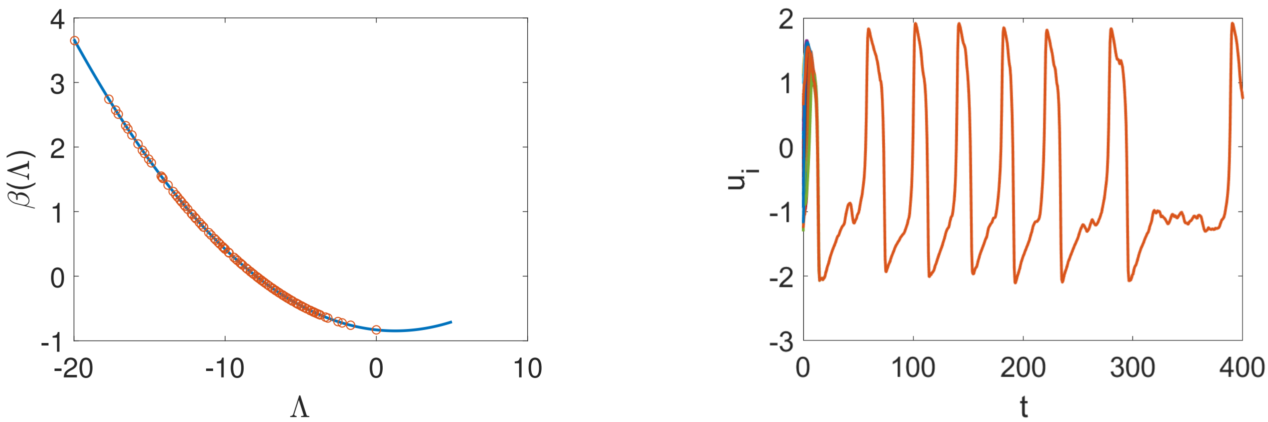

(a) **(b)**

Figure 4. Determinant-based spectral indicator and stochastic response of system (3.1) when $D_1 = 0$, $D_2 = 0.1$, and $I = 0.25$. (a) The determinant indicator $\beta(\Lambda) = \det M(\Lambda)$ as a function of the Laplacian eigenvalue Λ; the marked points denote the graph eigenvalues Λ_k. (b) Representative node time series showing the finite-network stochastic response. The fixed parameters are $a = 0.7$, $b = 0.8$, $\varepsilon = 0.08$, $n = 100$, $d_1 = d_2 = 0.1$, and $I = 0.25$.

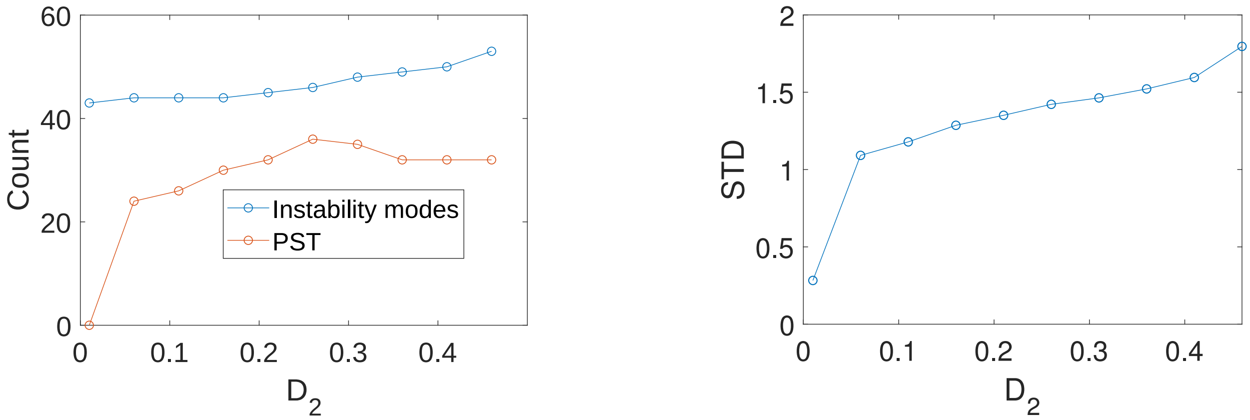

(a) **(b)**

Figure 5. Noise-intensity dependence for recovery-channel noise when $D_1 = 0$. (a) Diagnostic curves for the number of determinant-unstable modes N^{β}_{unst}, defined by $\beta(\Lambda_k) < 0$, and the potential switching count PST as functions of D_2. (b) Diagnostic curve for STD as a function of D_2. The left vertical axis is labeled "Count", and the right vertical axis is labeled "STD", consistently with (3.5). The fixed parameters are $a = 0.7$, $b = 0.8$, $\varepsilon = 0.08$, $n = 100$, $d_1 = d_2 = 0.1$, and $I = 0.25$. Here N^{β}_{unst} counts the graph modes satisfying $\beta(\Lambda_k) < 0$, PST counts the episodes in which STD rises above 10^{-2} and subsequently returns below this threshold, and STD measures the node-to-node dispersion of the membrane-potential variable u.

Figures 6–10 summarize the noise-dependent determinant boundaries. The curves denoted by λ_4 and λ_5 are the two roots of $\beta(\Lambda; D_1, D_2) = 0$, as defined in (2.21), and delimit the interval in Λ where $\beta(\Lambda) < 0$. If a graph eigenvalue lies between these two roots, it is counted in N^{β}_{unst}. These panels therefore provide the connection between multiplicative-noise intensity and the plotted determinant instability interval. The accompanying time-series panels illustrate the nonlinear stochastic response after graph modes enter this interval.

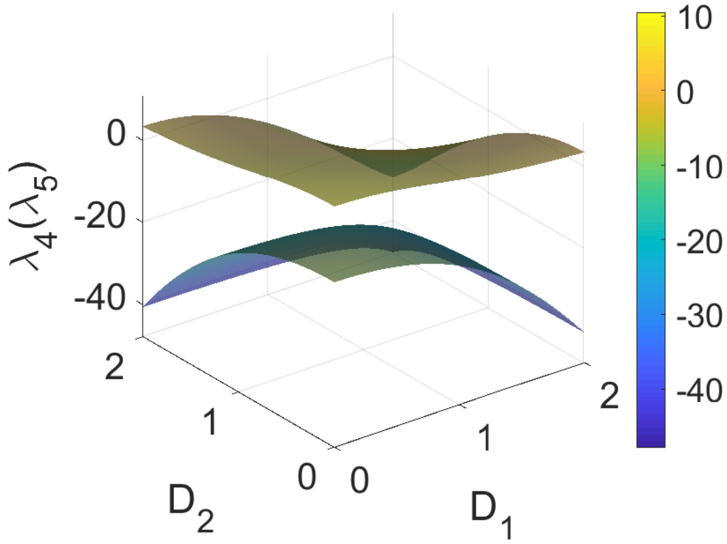

Figure 6. Noise-dependent determinant boundary in the (D_1, D_2) plane. The two surfaces $\lambda_4(D_1, D_2)$ and $\lambda_5(D_1, D_2)$ are the roots of $\beta(\Lambda; D_1, D_2) = 0$ and delimit the interval of Laplacian eigenvalues for which $\beta(\Lambda) < 0$. Since $\lambda_4 < \lambda_5$, the lower surface corresponds to λ_4, whereas the upper surface corresponds to λ_5. The fixed parameters are $a = 0.7$, $b = 0.8$, $\varepsilon = 0.08$, $n = 100$, $d_1 = d_2 = 0.1$, and $I = 0.25$.

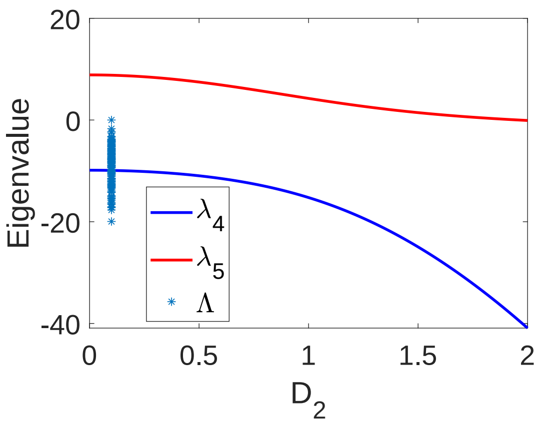

(a)

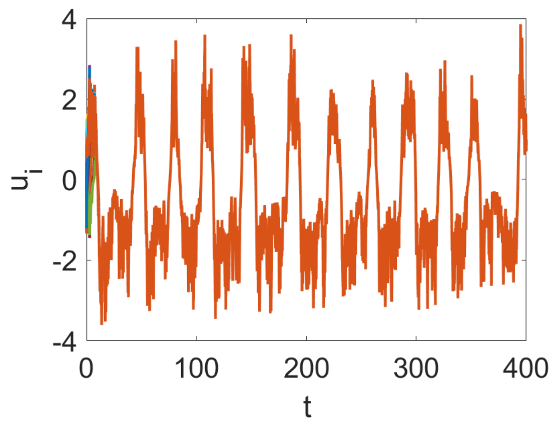

(b)

Figure 7. Noise-dependent determinant interval and corresponding stochastic response. (a) Roots λ_4 and λ_5 of $\beta(\Lambda) = 0$ as functions of D_2 when $D_1 = 0.6$; the overlaid graph eigenvalues Λ_k falling between the two roots satisfy $\beta(\Lambda_k) < 0$. (b) Representative node time series when $D_1 = 0.6$ and $D_2 = 0.1$. The left vertical axis is labeled "Eigenvalue". The fixed parameters are $a = 0.7$, $b = 0.8$, $\varepsilon = 0.08$, $n = 100$, $d_1 = d_2 = 0.1$, and $I = 0.25$.

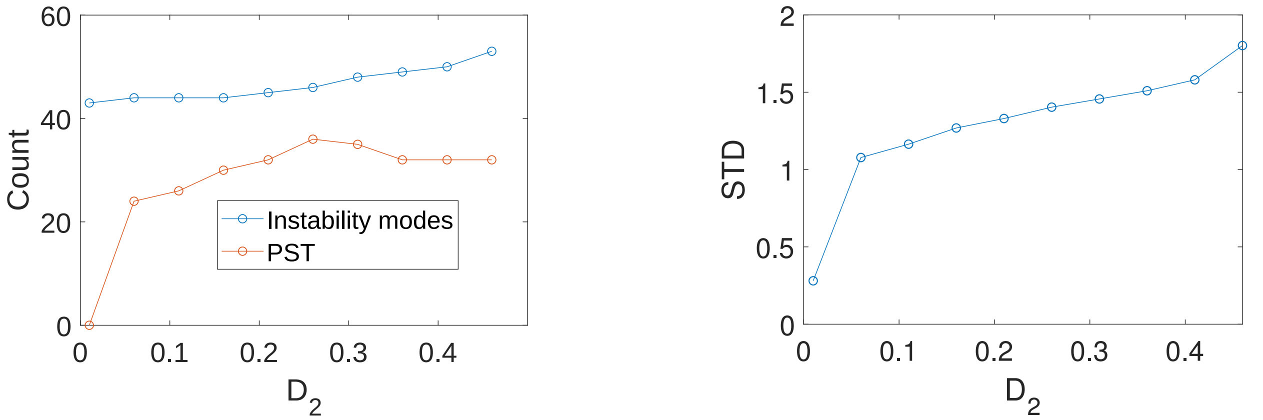

(a) **(b)**

Figure 8. Noise-intensity dependence when $D_1 = 0.01$. (a) Diagnostic curves for the number of determinant-unstable modes N^{β}_{unst}, defined by $\beta(\Lambda_k) < 0$, and the potential switching count PST as functions of D_2. (b) Diagnostic curve for STD as a function of D_2. The left vertical axis is labeled "Count", and the right vertical axis is labeled "STD", consistently with (3.5). The fixed parameters are $a = 0.7$, $b = 0.8$, $\varepsilon = 0.08$, $n = 100$, $d_1 = d_2 = 0.1$, and $I = 0.25$. Here N^{β}_{unst} counts the graph modes satisfying $\beta(\Lambda_k) < 0$, PST counts the episodes in which STD rises above 10^{-2} and subsequently returns below this threshold, and STD measures the node-to-node dispersion of the membrane-potential variable u.

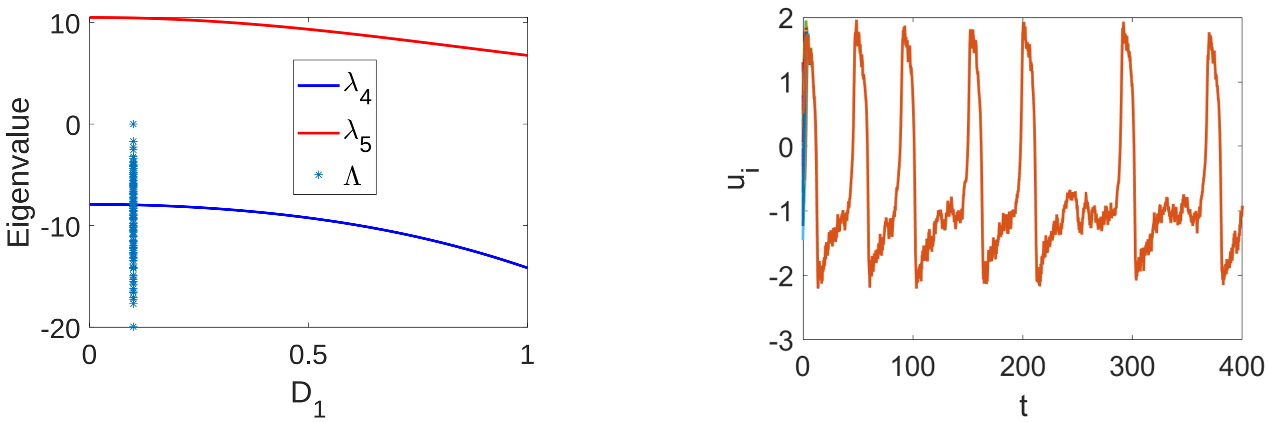

(a) **(b)**

Figure 9. Noise-dependent determinant interval and corresponding stochastic response. (a) Roots λ_4 and λ_5 of $\beta(\Lambda) = 0$ as functions of D_1 when $D_2 = 0.01$; the overlaid graph eigenvalues Λ_k indicate which modes satisfy $\beta(\Lambda_k) < 0$. (b) Representative node time series when $D_1 = 0.1$ and $D_2 = 0.01$. The left vertical axis is labeled "Eigenvalue". The fixed parameters are $a = 0.7$, $b = 0.8$, $\varepsilon = 0.08$, $n = 100$, $d_1 = d_2 = 0.1$, and $I = 0.25$.

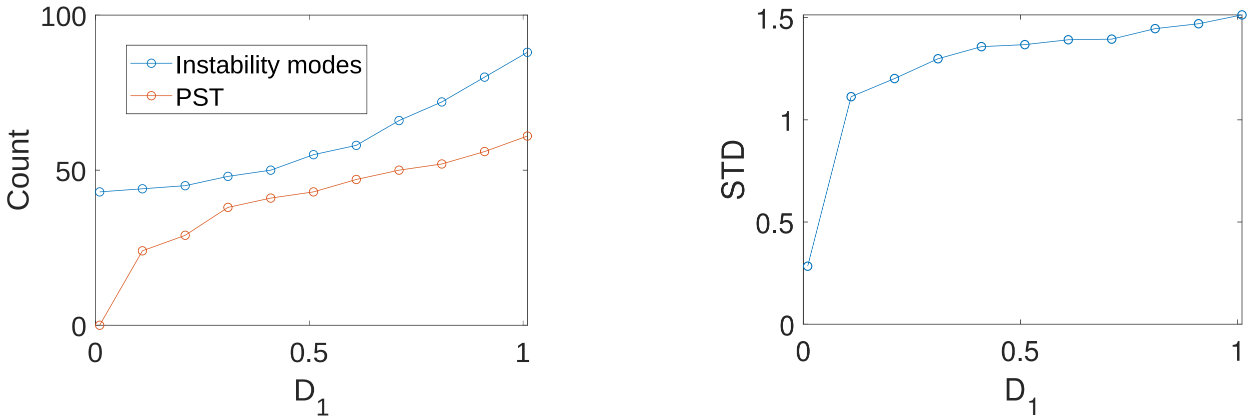

(a) **(b)**

Figure 10. Noise-intensity dependence when $D_2 = 0.01$. (a) Diagnostic curves for the number of determinant-unstable modes N^{β}_{unst}, defined by $\beta(\Lambda_k) < 0$, and the potential switching count PST as functions of D_1. (b) Diagnostic curve for STD as a function of D_1. The left vertical axis is labeled "Count", and the right vertical axis is labeled "STD", consistently with (3.5). The fixed parameters are $a = 0.7$, $b = 0.8$, $\varepsilon = 0.08$, $n = 100$, $d_1 = d_2 = 0.1$, and $I = 0.25$. Here N^{β}_{unst} counts the graph modes satisfying $\beta(\Lambda_k) < 0$, PST counts the episodes in which STD rises above 10^{-2} and subsequently returns below this threshold, and STD measures the node-to-node dispersion of the membrane-potential variable u.

Figures 11 and 12 quantify synchronization-related behavior in the oscillatory regime $I = 0.5$. These plots are not part of the equilibrium-based spectral stability test at $I = 0.25$. They are included to show how noise changes synchronization timing once the local FHN kinetics already supports oscillatory activity. No comparison with clinical EEG is made in the revised manuscript, and no mechanistic conclusion about epileptic seizures is drawn.

Figure 13 complements the representative trajectories with an ensemble-level uncertainty assessment. The median and empirical 95% band show the run-to-run variability explicitly, while the time-step panel shows overlapping confidence intervals for all three tested steps. This check supports the use of $\Delta t = 0.01$ for the reported finite-network diagnostic, although it does not replace a convergence analysis for every point in a full parameter sweep.

Figure 14 additionally averages over both random graph realizations and Brownian paths. It confirms a clear increase in the determinant-unstable mode count as D_1 increases, while also showing that trajectory-based quantities such as PST and STD have appreciably larger sampling variability. Conclusions concerning these latter diagnostics are therefore based on ensemble trends and confidence intervals rather than on individual nonmonotone sample values.

Overall, the numerical evidence is consistent with the revised theoretical claim: multiplicative noise shifts the determinant-based component of the conservative mean-square spectral boundary and changes synchronization/heterogeneity in a finite FHN network. A stronger claim about classical spatial Turing patterns would require spatially ordered networks or lattices, explicit modal-amplitude plots, systematic diffusivity-ratio scans, and wave-number-dependent boundary diagrams.

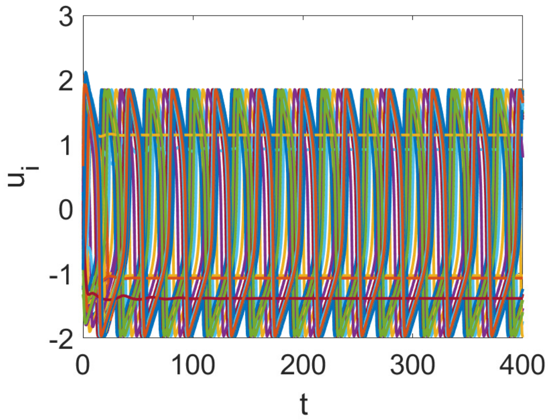

(a)

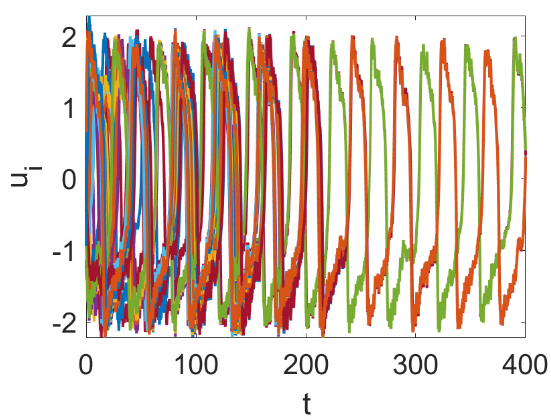

(b)

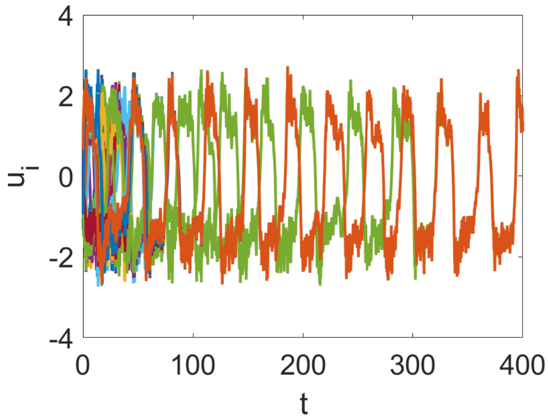

(c)

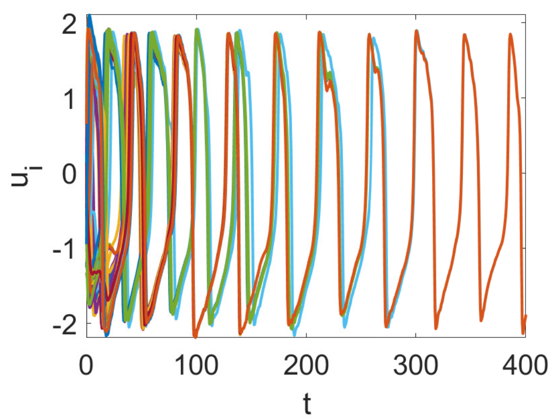

(d)

Figure 11. Representative stochastic synchronization responses of system (3.1) in the oscillatory regime $I = 0.5$. (a) Node time series without multiplicative noise, $D_1 = D_2 = 0$. (b) Node time series under direct noise, $D_1 = 0.1$ and $D_2 = 0$. (c) Node time series under stronger direct noise, $D_1 = 0.2$ and $D_2 = 0$. (d) Node time series under recovery-channel noise, $D_1 = 0$ and $D_2 = 0.1$. The fixed parameters are $a = 0.7$, $b = 0.8$, $\varepsilon = 0.08$, $n = 100$, and $d_1 = d_2 = 0.1$.

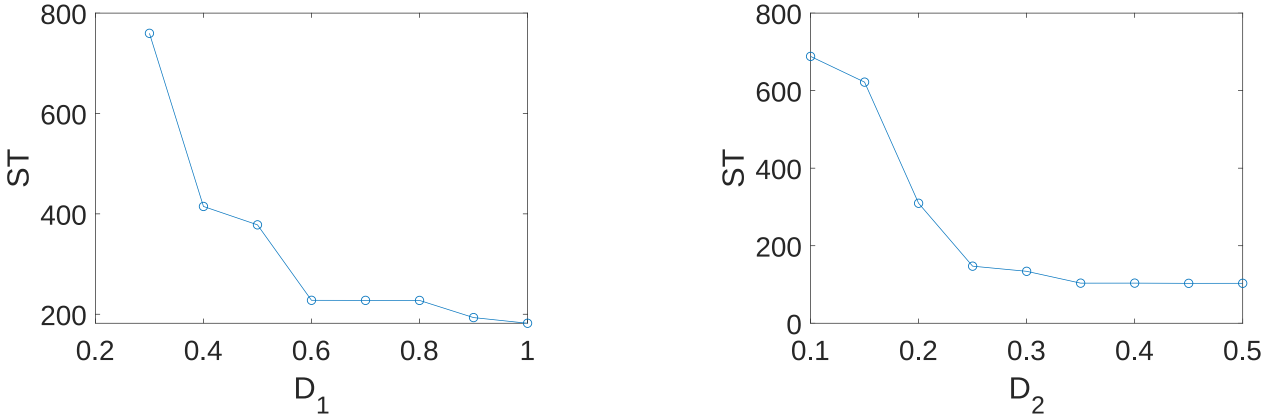

(a) **(b)**

Figure 12. Synchronization diagnostics in the oscillatory regime $I = 0.5$. (a) Diagnostic curve for the synchronization time ST as a function of D_1 when $D_2 = 0$. (b) Diagnostic curve for ST as a function of D_2 when $D_1 = 0$. Both vertical axes are labeled "ST". The fixed parameters are $a = 0.7$, $b = 0.8$, $\varepsilon = 0.08$, $n = 100$, and $d_1 = d_2 = 0.1$. Here ST is the first time after which STD $\leq 10^{-3}$ remains satisfied for the rest of the simulated interval.

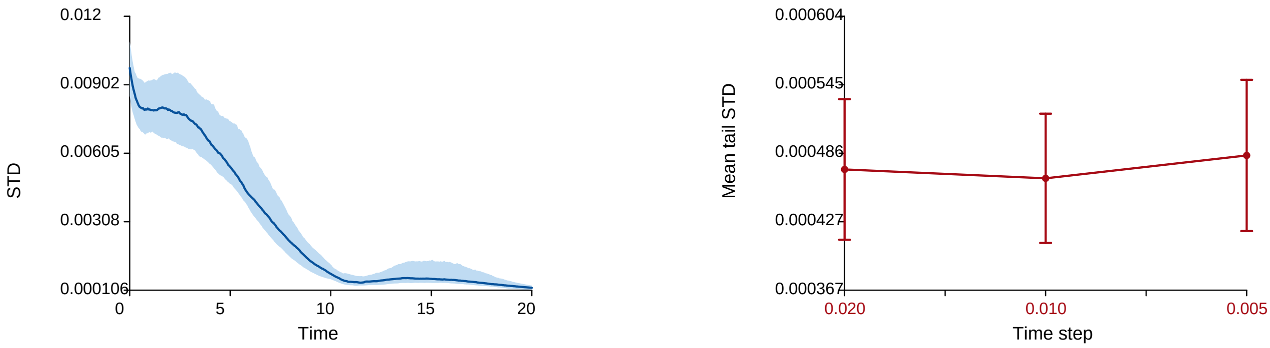

(a) **(b)**

Figure 13. Ensemble and numerical-resolution validation for system (3.1) at $I = 0.25$, $D_1 = 0.1$, and $D_2 = 0$. (a) Median STD(t) (solid line) and pointwise 2.5–97.5 percentile band (shading) from 30 independent stochastic realizations at the baseline step $\Delta t = 0.01$. (b) Ensemble mean of the time-averaged STD over $15 \leq t \leq 20$ for $\Delta t = 0.02$, 0.01, and 0.005; error bars show 95% confidence intervals across realizations. Fixed parameters are $a = 0.7$, $b = 0.8$, $\varepsilon = 0.08$, $n = 100$, $p = 0.05$, and $d_1 = d_2 = 0.1$. The graph is held fixed across the time-step comparison.

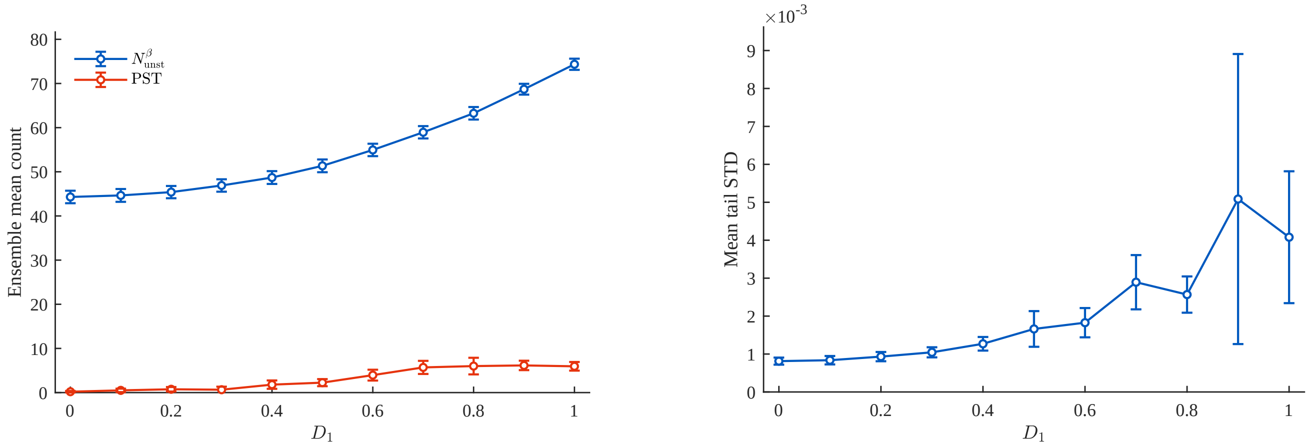

(a) **(b)**

Figure 14. Independent graph-and-Brownian ensemble validation for direct noise with $D_2 = 0$. (a) Ensemble means and 95% confidence intervals for N^{β}_{unst} and PST. (b) Ensemble mean and 95% confidence interval for the time-averaged STD over $10 \le t \le 15$. At each $D_1 = 0, 0.1, \ldots, 1.0$, statistics use 20 independent connected Erdős–Rényi graphs $G(100, 0.05)$ and independent Brownian paths. Fixed parameters are $a = 0.7$, $b = 0.8$, $\varepsilon = 0.08$, $I = 0.25$, $d_1 = d_2 = 0.1$, and $\Delta t = 0.01$.

4. Conclusions

This work analyzed multiplicative-noise effects in a network-coupled FitzHugh–Nagumo system from the viewpoint of mean-square spectral stability. The stochastic formulation was revised to use independent node- and variable-specific Brownian motions, and the noise amplitudes were chosen to vanish at the homogeneous equilibrium. The graph coupling sign was fixed by setting $L = \mathcal{A} - \mathcal{D}$ and adding dL to the reaction kinetics, which corresponds to standard dissipative diffusion.

We distinguished the exact mean-square stability problem, governed by the Kronecker operator $\mathcal{K}$, from the explicit $P = I$ Lyapunov bound. We also defined mean-square Turing-type instability through exponential growth of the heterogeneous projected second moment and clarified that $s(\mathcal{K}) > 0$ alone establishes total mean-square instability, not spatial mode selection. The $P = I$ bound yields a simple mode-wise matrix $M(\Lambda_k)$ and a conservative spectral boundary depending on D_1, D_2, d_1, d_2, the external current I, and the graph eigenvalues. For the adopted FHN parameters, the trace-driven branch can occur only when both noise channels are sufficiently strong; it first destabilizes the homogeneous mode and is absent in all one-channel sweeps. These qualifications remove the previous overstatement that a positive eigenvalue of $J^T + J + \sum B_r^T B_r$ is automatically a necessary-and-sufficient instability criterion.

The simulations support the revised claim at a qualitative level: direct noise acting on the u-component more strongly enlarges the determinant-negative interval and increases N^{β}_{unst}, whereas recovery-channel noise changes variability and synchronization in a more gradual way. The added exact-versus-$P = I$ comparison demonstrates directly that the Euclidean Lyapunov test can fail to certify systems that remain exactly mean-square stable. The fixed-graph ensemble, time-step check, and independent graph-and-Brownian ensemble quantify both numerical uncertainty and sample-to-sample fluctuations; the latter are appreciably larger for trajectory-based PST and STD than for the spectrum-based mode count. The plotted trajectories and synchronization diagnostics should be read as stochastic responses of finite networks, not as stand-alone proof of classical spatial Turing patterns or as evidence for clinical seizure mechanisms. Future work should add spatially ordered networks or lattices, modal-amplitude diagnostics, broader ensemble validation across the parameter plane, systematic diffusivity-ratio and external-current sweeps, and possible time-delay effects in order to connect the present mean-square spectral theory more directly with classical wave-number-dependent Turing pattern formation.

Author contributions

Bing Zhou: Conceptualization, Methodology, Software, Investigation, Formal analysis, Writing–original draft; Manrui Zhou: Data curation, Writing–original draft; Xiangrong Liu: Visualization, Investigation; Qianqian Zheng: Resources, Supervision. All authors have read and approved the final version of the manuscript for publication.

Use of Generative-AI tools declaration

The authors declare they have not used Artificial Intelligence (AI) tools in the creation of this article.

Acknowledgments

This work was supported by the Program for Innovative Research Team of Zhongyuan Institute of Science and Technology (ZYKJCXTD202403).

Conflict of interest

The authors declare that there is no conflict of interests.

Data availability statements

The numerical simulations are reproducible from the model equations, graph-generation rule, independent Brownian increments, time step, thresholds, and parameter settings stated in the manuscript. Simulation scripts, graph-generation code, and random seeds are available from the corresponding author upon reasonable request.

References

1. J. D. Murray, *Mathematical biology II: spatial models and biomedical applications*, 3 Eds., New York: Springer, 2003. https://doi.org/10.1007/b98869
2. M. X. Chen, X. Z. Li, C. R. Tian, Determining Turing instability of the periodic solution of a predator–prey model, *Appl. Math. Lett.*, **171** (2025), 109689. https://doi.org/10.1016/j.aml.2025.109689

3. M. X. Chen, Pattern dynamics of a Lotka-Volterra model with taxis mechanism, *Appl. Math. Comput.*, **484** (2025), 129017. https://doi.org/10.1016/j.amc.2024.129017

4. A. M. Turing, The chemical basis of morphogenesis, *Phil. Trans. R. Soc. B*, **237** (1952), 37–72. https://doi.org/10.1098/rstb.1952.0012

5. H. Nakao, A. S. Mikhailov, Turing patterns in network-organized activator-inhibitor systems, *Nature Phys.*, **6** (2010), 544–550. https://doi.org/10.1038/nphys1651

6. M. Asllani, J. D. Challenger, F. S. Pavone, L. Sacconi, D. Fanelli, The theory of pattern formation on directed networks, *Nat. Commun.*, **5** (2014), 4517. https://doi.org/10.1038/ncomms5517

7. S. Mimar, M. Asllani, J. D. Challenger, D. Fanelli, Turing patterns mediated by network topology in homogeneous active systems, *Phys. Rev. E*, **99** (2019), 062303. https://doi.org/10.1103/PhysRevE.99.062303

8. Q. Q. Zheng, J. W. Shen, Y. Xu, Turing instability in the reaction-diffusion network, *Phys. Rev. E*, **102** (2020), 062215. https://doi.org/10.1103/PhysRevE.102.062215

9. T. Butler, N. Goldenfeld, Fluctuation-driven Turing patterns, *Phys. Rev. E*, **84** (2011), 011112. https://doi.org/10.1103/PhysRevE.84.011112

10. T. Biancalani, L. Dyson, A. J. McKane, Noise-induced Turing patterns: Physical mechanisms and scaling laws, *Phys. Rev. Lett.*, **112** (2014), 038101. https://doi.org/10.1103/PhysRevLett.112.038101

11. X. H. Xu, J. Y. Zhang, W. H. Zhang, Mean square exponential stability of stochastic neural networks with reaction-diffusion terms and delays, *Appl. Math. Lett.*, **24** (2011), 5–11. https://doi.org/10.1016/j.aml.2010.07.002

12. R. Xiao, Q. Y. Gao, S. Azaele, Y. Z. Sun, Effects of noise on the critical points of Turing instability in complex ecosystems, *Phys. Rev. E*, **108** (2023), 014407. https://doi.org/10.1103/PhysRevE.108.014407

13. Z. Q. Wang, Y. Xu, Y. G. Li, T. Kapitaniak, J. Kurths, Chimera states in coupled Hindmarsh-Rose neurons with α-stable noise, *Chaos Soliton. Fract.*, **148** (2021), 110976. https://doi.org/10.1016/j.chaos.2021.110976

14. M. Asllani, T. Biancalani, D. Fanelli, Stochastic Turing patterns on a network, *Phys. Rev. E*, **86** (2012), 046105. https://doi.org/10.1103/PhysRevE.86.046105

15. F. Yu, X. Q. Wang, Y. Xiao, Y. He, W. Yao, S. Cai, et al., Extreme multistability in discrete memristive neuron maps and implications for dual-field applications, *Integration*, **109** (2026), 102688. https://doi.org/10.1016/j.vlsi.2026.102688

16. F. Yu, X. Q. Wang, R. Y. Guo, Z. J. Ying, Y. He, Q. Zou, Discrete neuron models and memristive neural network mapping: A comprehensive review, *Chinese Phys. B*, **34** (2025), 120501. https://doi.org/10.1088/1674-1056/ae0a3b

17. F. Yu, R. Y. Guo, M. F. Zheng, W. Yao, D. D. Zhang, S. Cai, Novel approach to time series forecasting based on memristive Hopfield Neural Network with hidden heterogeneous and homogeneous extreme multistability, *Chaos Soliton. Fract.*, **210** (2026), 118626. https://doi.org/10.1016/j.chaos.2026.118626

18. A. A. Faisal, L. P. J. Selen, D. M. Wolpert, Noise in the nervous system, *Nat. Rev. Neurosci.*, **9** (2008), 292–303. https://doi.org/10.1038/nrn2258
19. M. D. McDonnell, L. M. Ward, The benefits of noise in neural systems: Bridging theory and experiment, *Nat. Rev. Neurosci.*, **12** (2011), 415–425. https://doi.org/10.1038/nrn3061
20. M. Masoliver, N. Malik, E. Schöll, A. Zakharova, Coherence resonance in networks of FitzHugh-Nagumo systems, *Chaos*, **27** (2017), 101102. https://doi.org/10.1063/1.5003237
21. L. Colombani, P. Toulouse, Propagation of chaos in FitzHugh-Nagumo mean field networks, *Mathematical Neuroscience and Applications*, **3** (2023), 1–50. https://doi.org/10.46298/mna.9748
22. M. Gerster, R. Berner, J. Sawicki, A. Zakharova, A. Škoch, J. Hlinka, et al., FitzHugh-Nagumo oscillators on complex networks mimic epileptic-seizure-related synchronization phenomena, *Chaos*, **30** (2020), 123130. https://doi.org/10.1063/5.0021420
23. T. Chouzouris, I. Omelchenko, A. Zakharova, J. Hlinka, P. Jiruska, E. Schöll, Chimera states in brain networks: Empirical neural vs. modular fractal connectivity, *Chaos*, **28** (2018), 045112. https://doi.org/10.1063/1.5009812
24. J. Cubillos-Cornejo, M. E. Mendoza, I. Bordeu, Extreme events at the onset of epileptic-like intermittent activity of FitzHugh–Nagumo oscillators on small-world networks, *Chaos Soliton. Fract.*, **192** (2025), 116000. https://doi.org/10.1016/j.chaos.2025.116000
25. Z. H. Wang, Z. H. Liu, A Brief Review of Chimera State in Empirical Brain Networks, *Front. Physiol.*, **11** (2020), 724. https://doi.org/10.3389/fphys.2020.00724
26. R. G. Andrzejak, C. Rummel, F. Mormann, K. Schindler, All together now: Analogies between chimera state collapses and epileptic seizures, *Sci. Rep.*, **6** (2016), 23000. https://doi.org/10.1038/srep23000
27. F. Han, D. G. Fang, L. Y. Zhang, Q. Y. Wang, Neurological disease and cognitive dynamics (I): Dynamics and control of epileptic seizures, *Advances in Mechanics*, **52** (2022), 339–396. https://doi.org/10.6052/1000-0992-21-064
28. L. Y. Zhang, Q. Y. Wang, G. Baier, Spontaneous transitions to focal-onset epileptic seizures: A dynamical study, *Chaos*, **30** (2020), 103114. https://doi.org/10.1063/5.0021693
29. S. G. Hou, X. T. Liu, Y. Yu, Q. Y. Wang, Functional modal feature analysis based on the network transition dynamics of epileptic seizure, *Chaos Soliton. Fract.*, **197** (2025), 116500. https://doi.org/10.1016/j.chaos.2025.116500
30. J. Y. Zhao, Q. Y. Wang, Y. Yu, A new pathway for controlling absence seizures by reducing GABA uptake from astrocytes: a dynamical perspective, *Commun. Nonlinear Sci.*, **149** (2025), 108929. https://doi.org/10.1016/j.cnsns.2025.108929
31. M. Kantner, E. Schöll, S. Yanchuk, Delay-induced patterns in a two-dimensional lattice of coupled oscillators, *Sci. Rep.*, **5** (2015), 8522. https://doi.org/10.1038/srep08522

AIMS Press